
Article:
de Sá, J.S., Jacklin, R., Gomes, J.A.C.P. et al. (1 more author) (2023) Formation and Protectiveness of Fe/Ca Carbonate Layer on X80 Steel in High-Pressure CO_2 Corrosion Environments. Corrosion, 79 (7). pp. 782-789. ISSN 0010-9312

https://doi.org/10.5006/4248

Formation and protectiveness of Fe/Ca carbonate layer on X80 steel in high pressure CO_2 corrosion environments

Jonas S. de Sá ‡,, Robert Jacklin **, José A. C. P. Gomes * and Richard Barker ***

‡Corresponding author. E-mail: jonas.sa@coppe.ufrj.br

*Metallurgical and Materials Engineering Program, Federal University of Rio de Janeiro, Rio de Janeiro 21941-598, Brazil.

**School of Mechanical Engineering, University of Leeds, Leeds LS2 9JT, United Kingdom.

ABSTRACT

The effect of calcium ions (Ca^{2+}) on corrosion of API 5L X80 carbon steel in carbon dioxide (CO_2)-saturated brines was studied. Tests were carried out in brines containing 0, 1000 or 5000 ppm of calcium ions with a constant chloride ion concentration, at temperatures of 35 and 60 °C, and pressure of 80 bar. The corrosion rates were determined by mass loss, and the protective properties of the film was evaluated by carrying out electrochemical measurements in a separate vessel containing a standard brine. The results showed that adding Ca^{2+} to the brine slightly reduced the average corrosion rate, even in the absence of a crystalline corrosion product scale. For longer exposure times, it promoted the growth of a mixed iron-calcium carbonate ($Fe_xCa_yCO_3$) scale with increasing calcium molar mass, shifting the scale morphology from prismatic crystals (pure $FeCO_3$) to globular (mixed carbonate). At 35 °C the mixed iron-calcium carbonate scale offered better protection when compared to the pure $FeCO_3$ scale counterpart. However, at 60 °C, where a thicker carbonate scale was formed, the increase of Ca^{2+} content had a minimal effect on the corrosion rate.

KEY WORDS: *Calcium carbonate; CO_2 corrosion; High temperature; Iron carbonate; Mixed carbonate*.

1 INTRODUCTION

Carbon capture and storage (CCS) technology is a feasible and economic way to reduce greenhouse gas emissions. It consists of capturing CO_2 from high-emission sources, such as fossil fuel power plants, compressing it into a liquid or supercritical state and transporting it to a storage site for sequestration or to enhance oil recovery (EOR). In EOR operations, CO_2 and brine may be alternately flooded into the injection wells. In this scenario, the injection lines may periodically be exposed to a saline solution saturated with supercritical CO_2. This process is most commonly performed using carbon steel pipelines due to their low cost and widespread availability, despite their low corrosion resistance. It is well-known that when carbon steel is exposed to water and CO_2, the main by-product is the formation of an iron carbonate ($FeCO_3$) film on the steel surface. Such surface products are of great importance, as they can block active sites on the steel surface and act as a diffusion barrier to electrochemically active species, reducing corrosion under certain conditions, and prolonging the lifetime of downhole equipment and production lines. [1–5]

Sun and Nesic's [6] semi-empirical precipitation rate model (Equation 1) describes the temperature dependence of scale formation, where PR is the precipitation rate, A/V is the surface area-to-volume ratio, k_r is the kinetic constant, K_{sp} is the solubility product and SS is the supersaturation. Both k_r and K_{sp} are functions of temperature, at low temperatures the Fe^{2+} and CO_3^{2-} have a low kinetic constant and high solubility limit. On the other hand, as the temperature increases, the kinetic constant increases, and the saturation of the solution is reached at lower ion activities, leading to the precipitation of $FeCO_3$ crystals. This precipitation can form a dense and protective corrosion product scale on the

steel surface, which blocks active sites on the steel surface and can potentially hinder mass-transfer between the bulk and the steel surface, decreasing the corrosion rate. Zhang et al. [7] have reported this trend, where they assessed the corrosion rates of API 5L X65 steel under static supercritical CO_2 conditions and found that the corrosion rate increased from 50 to 80 ^oC and then decreased from 80 to 130 ^oC, coinciding with the onset of precipitation.

$$PR = \frac{A}{V} k_r K_{sp} (SS - 1) \quad (1)$$

Additionally, typical reservoir brines can have a complex chemical composition that may include Cl^-, Na^+, Mg^{2+} and Ca^{2+}, among other ions. The presence of divalent cations has been shown to facilitate the precipitation of mixed carbonates, such as iron-calcium carbonate ($Fe_xCa_yCO_3$, where x+y=1). This results in carbonates with distinct morphological and chemical properties when compared to the pure counterparts [2,7–12]. Literature discussing the effect of Ca^{2+} on CO_2 corrosion of carbon steel often appears contradictory. Esmaeely et al. [13,14] reported that at low Ca^{2+} concentrations the corrosion rate decreased with time due to the formation of a protective scale. However, at high concentrations of Ca^{2+} the corrosion rate increased with time due to formation of a non-protective scale, attributed this effect to Ca^{2+} rather than Cl^-. Shamsa et al. [1] reported that the addition of Ca^{2+} resulted in the formation of a thicker and less protective corrosion product layer consisting of $Fe_xCa_yCO_3$, but these effects were smaller at higher temperatures. Hua et al. [2] observed that at 100 bar and 60 ^oC the addition of Ca^{2+} (from 0 to 10000 ppm) reduced the general corrosion rate of carbon steel in the beginning of the tests, but the values converged for longer exposure times (up to 96 h). They also observed that Ca^{2+} was more likely to co-precipitate in conjunction with $FeCO_3$ compared to Mg^{2+}. Tavares et al. [8] observed that although the presence of $CaCO_3$ decreased the general corrosion rate, the mixed carbonate films exhibited greater porosity, which could result in increased localized corrosion.

Despite more complex brine chemistries existing in the field, most research on CO_2 corrosion of carbon steel is directed towards NaCl solutions and lower pressures than those considered in this study, while limited research has focused on the effect of Ca^{2+}. Additionally, most tests are carried in a closed system with evolving chemistries and pH over time. Hence, it is challenging to determine the true protectiveness of the corrosion product when the corrosion rate is influenced by both pH and film formation. In this context, this study investigated the effect of Ca^{2+} on the CO_2 corrosion of an API 5L X80 carbon steel in CO_2-saturated brines at 80 bar and 35 or 60 ^oC, using a two-stage testing procedure where the scale is formed in an autoclave before being transferred to a fresh standard brine to evaluate the protective nature of the corrosion products.

2 EXPERIMENTAL PROCEDURE

The material used in this study was an API 5L X80 steel with yield strength and ultimate tensile strength of 581 and 628 MPa, respectively, and a chemical composition of (wt.%): 0.041%C, 1.56%Mn, 0.010%P, 0.001%S, 0.300%Si, 0.251%Ni, 0.057%Cr, 0.201%Mo, 0.001%V, 0.037%Nb and Fe in balance. Test samples were machined to have the dimensions 22 x 9 x 3 mm^3, with a 2 mm diameter hole for mounting. All the samples were wet ground by successive silicon carbide paper up to P800 grit size. Then they were degreased with acetone, washed with deionised water, dried before weighing using an electronic balance (accuracy of 0.01 mg) and stored in a desiccator until use.

Immersion corrosion tests were carried out in a 1 L Hastelloy C276 autoclave, where six samples were fixed in a PEEK sample holder, as shown in Figure 1. Tests were carried out in supercritical CO_2-saturated brines using the test conditions listed in Table 1, where each test condition

was carried out twice. The test solutions were prepared using deionized water and analytical grade reagents, and the contents were balanced so that it contained 0, 1000 or 5000 ppm of Ca^{2+} and maintained a constant chloride ion concentration. Once saturated with CO_2, 600 mL of the brine was transferred to the autoclave, then the autoclave was pressurized up to 30 bar using CO_2 and vented twice to purge any oxygen from the system. Subsequently, the autoclave was pressurised to 80 bar and heated to the desired temperature. At the end of each test, the samples were removed from the autoclave as quickly as possible to reduce the exposure time in the solution after depressurisation. They were then rinsed with deionized water, and dried with compressed air. Three samples from each test were selected for mass loss measurement. They were weighed, chemically cleaned using Clarke's solution (20 g antimony trioxide, 50 g stannous chloride and 1000 ml hydrochloric acid) to remove corrosion products, and then rinsed and dried one more time, before weighed again. The average corrosion rate by mass loss measurements was determined using Equation 2 [15], where Δm is the mass difference in g, ρ is the material density in g/cm^3, A is the sample surface area in cm^2, t is the test duration in hours and C_{rate} is the corrosion rate in mm/year.

$$C_{rate} = \frac{87600\ \Delta m}{\rho\ A\ t} \quad (2)$$

As the test time progresses, the species formed/consumed in the corrosion reactions are expected to change the brine chemistry, surface pH and bulk pH over time [16]. Such that at the end of the test period the test cell will have a complex chemical composition which is highly dependent on the initial conditions. This scenario would impose a challenge to compare the corrosion scales formed under different test conditions. Therefore, to eliminate the influence from the final brine chemistry, after exposure to the conditions listed in Table 1, one of the corroded samples was transferred to a static glass cell containing 1 L of a standardized brine (CO_2-saturated 30 g/L NaCl solution at 25 ^{o}C, atmospheric pressure and pH 3.8). The electrochemical properties of the corrosion scales were investigated using linear polarization resistance (LPR) and potentiodynamic polarization techniques, where the pre-corroded samples were used as working electrodes (WE), a platinum wire as counter electrode (CE) and an Ag/AgCl (1M KCl) reference electrode (RE). A potentiostat was used to run LPR and potentiodynamic sweeps, the measurements started 10 min after immersion, following the sequence of LPR (twice), followed by cathodic then anodic polarization sweeps with a 5 min rest period between each measurement. The average corrosion rate (in mm/year) by electrochemical measurements was determined using Equation 3 [17], where M_{Fe} is the iron atomic mass in g/mol, n is the number of electrons transferred in the reaction, ρ is the material density in g/cm^3, A is the working electrode exposed area in cm^2 and i_{corr} is the corrosion current density in A/cm^2 determined by Equation 4 [17], where R_p is the polarization resistance in ohm·cm^2. The polarization resistance (R_p) was determined by LPR measurements, which were made using a scan rate of 0.2 mV/s in the potential range of E_{corr} ± 15 mV. The response is approximately a straight line where the slope is the polarization resistance (R_p). Potentiodynamic measurements were used to determine the anodic (β_a) and cathodic (β_c) Tafel constants, in V/decade.

$$C_{rate} = \frac{3270\ i_{corr}\ M_{Fe}}{n\ \rho\ A} \quad (3)$$

$$i_{corr} = \frac{\beta_a \beta_c}{2.303\ (\beta_a + \beta_c) R_p} \quad (4)$$

The surface morphology of the samples was observed using a Carl Zeiss EVO MA15 scanning electron microscope (SEM). The images were captured using secondary electron mode at an accelerating voltage of 20 kV at an average working distance of 8 mm. Cross section energy-

dispersive X-ray spectroscopy (EDX) line scans of the corrosion product were also prepared by coating one sample from each test with platinum before cutting a trench in the corrosion product layer using a FEI Nova200 dual beam FIB/SEM.

A Bruker D8 X-ray diffractometer was used to identify the phases and the molar fraction of Ca in $Fe_xCa_yCO_3$ using the Equation 5 [1]. This equation considers that the $FeCO_3$ and $CaCO_3$ share hexagonal lattice structure. Consequently, the introduction of Ca into $FeCO_3$ matrix will result in an increase of the d-spacing and shift the peak positions associated with the diffraction patterns of such crystalline planes towards lower values of 2θ. The peaks used in the equation were the most intense Bragg peaks for $CaCO_3$ and $FeCO_3$, which are located at 2θ positions 29.42° and 32.07° respectively, which correspond to the [104] inter-planar spacing. [1,14]

$$\frac{1}{d^2} = \frac{4}{3}\left(\frac{2.924y+26.626}{148.214y+582.680}\right) + \frac{16}{(1.688y+15.373)^2} \quad (5)$$

3 RESULTS AND DISCUSSION

3.1 Analysis of corrosion product morphology

Figure 2 shows the XRD patterns of the samples immersed in brines with different Ca^{2+} concentrations, temperature, and exposure time. The results of the samples tested at 35 °C exhibited typical α-iron peaks that can be associated with the steel substrate. Besides that, no peaks corresponding to a corrosion product surface film were detected on the samples that were immersed for 48 hours. In contrast, the XRD data for the samples exposed for 96 h exhibited sharp peaks, indicating that the corrosion product on the surface was crystalline. The peaks associated with the steel substrate were no longer present in the samples tested at 60 °C, suggesting that a thick corrosion scale prevented the x-rays from reaching the substrate.

Given that $FeCO_3$ and $CaCO_3$ share a hexagonal lattice structure, the introduction of Ca into $FeCO_3$ matrix shifts of the peak positions associated with the diffraction patterns of such crystalline planes towards lower values of 2θ. Based on this, Equation 5 can be used to calculate the mole fraction of Ca within the mixed iron-calcium carbonate from the shift in the (104) peak. The measured calcium content in the $Fe_xCa_yCO_3$ was 5.7 and 17.7 % for the samples immersed in the brines containing 1000 and 5000 ppm Ca^{2+} at 35 °C and 11.1 and 26.6 % for the brines containing 1000 and 5000 ppm Ca^{2+} at 60 °C and 80 bar for 96 h, respectively. Demonstrating the co-precipitation of $FeCO_3$ and $CaCO_3$, whilst showing that the ratio of carbonates in the scale composition is influenced by the brine composition. However, further work is required to determine the reason behind the increase of calcium content in the scale for higher temperatures.

Figure 3 shows SEM images of the surface of corroded X80 steel samples immersed in brines with different Ca^{2+}, temperature, and exposure time. XRD diffraction results for the samples exposed to the tested conditions for 48 h indicate no evidence of crystalline corrosion product, only the substrate α-Fe peaks could be identified. The surface morphology observed in the SEM images can be associated with a thin amorphous layer rich in Fe, C and O (based on EDX measurements) often reported in the literature [3], which appears to be more homogeneous as Ca^{2+} increases.

However, the samples that were exposed to longer immersion times (96 h) exhibited a partial coverage of prismatic crystals whose morphology is typical of carbonate crystals [1,2,8,13]. This also indicates that the surface scale might not be fully developed yet, and for exposure

times longer than considered in this study the film would have more opportunity to grow. In contrast, the higher temperature of 60 °C produced a full coverage of crystals significantly larger than the ones observed at 35 °C, which demonstrate that the precipitation and growth is much faster at higher temperatures.

The increase of Ca^{2+} concentration also promoted a change of crystal morphology after 96 h, where the flat surfaces of the crystals (Figure 3g) became less noticeable, shifting towards globular structures of similar size (Figure 3i). Hua et al. [2] previously reported similar morphology shifts when increasing the Ca^{2+} content in the brine from 0 to 10,000 ppm at 60 °C and 100 bar.

Figure 4 shows SEM images of the cross-sections of the corrosion product scales on X80 steel samples immersed in brines with various Ca^{2+} concentrations, temperature, and exposure time. The samples tested at 35 °C exhibited a highly porous corrosion product scale rich in Fe, C and O (based on EDX measurements). Despite the XRD measurements, only the sample exposed to the brine containing 5000 ppm Ca^{2+} showed traces of calcium in the corrosion product scale chemical composition based on EDX measurements. Voids at the interface between the corrosion product film and steel substrate indicate that the steel surface continued corroding under the film, indicative of film undermining [18], a process known in the literature to form porous and unprotective films. The corrosion product scales thicknesses measured within individual samples varied substantially, but the average thickness when exposed to the brines containing 0, 1000 and 5000 ppm Ca^{2+} was measured as 3.2, 5.3, 4.2 µm, respectively.

SEM images shows that the film formed at 60 °C is considerabley thicker (>100 µm) so the FIB technique was not adequate to prepare the cross section. Instead, the samples were mounted in epoxy resin then polished to reveal the film cross section. Cross section images show that the film is more compact than the ones formed at lower temperatures, some voids were still visible inside the film, but the amount decreased as the Ca^{2+} concentrations in the brine increased from 0 to 5000 ppm.

3.2 Corrosion rates obtained by mass loss tests

The average corrosion rate and corrosion product mass determined from mass loss measurements as a function of time and Ca^{2+} content in the brine for various conditions is shown in Figure 6. Results show that at 35 °C, the average corrosion rate reduces for longer exposure times, and for higher Ca^{2+} content in the brine. The corrosion rate after 48 h is higher (14.8, 13.3, 10.9 mm/year for the brines containing 0, 1000 and 5000 ppm Ca^{2+}, respectively) compared to after 96 h (14.5, 11.9, 9.8 mm/year for the brines containing 0, 1000 and 5000 ppm Ca^{2+}, respectively). The decrease of average corrosion rate in the brines containing a higher Ca^{2+} content seems to indicate that the presence of Ca^{2+} is either increasing the kinetics of corrosion scale formation or modifying the corrosion scale morphology to be more compact and protective. Additionally, the total scale mass increased from 0.008 to 0.011 g after 48h and from 0.021 to 0.036 g after 96h as the Ca^{2+} content in the brine increases from 0 to 5000 ppm. The decrease in corrosion rate in conjunction with an increase corrosion scale suggests that the precipitation and growth of the corrosion product scale for longer exposure times is assisting in the reduction of the average corrosion rates.

On the other hand, at 60 °C the corrosion rate and corrosion product mass on the steel surface remained relatively constant regardless of the Ca^{2+} content in the brine. The $FeCO_3$ precipitation rate is faster at higher temperatures due to the increased reaction rate, mass transport and lower solubility [19]. This is further supported by the significantly higher corrosion product mass measured at 60 °C. However, this shows that a thicker corrosion product layer may not necessarily correlate to a reduction of corrosion rate. This could be explained either due to a less protective scale despite its increased total mass, or that at 60 °C the corrosion rate in the first few hours was so high that it shifted the average

corrosion rate to higher values. The latter would indicate that these measurements may not be an accurate reflection of the corrosion rate in the presence of a protective corrosion product scale, i.e., the corrosion rate under these conditions is overestimated.

Also, the increased scale mass, despite similar mass losses at 35 and 60 ^{o}C after 96 h, suggests that more corrosion product is retained at the steel surface. It can be speculated that the faster corrosion kinetics at higher temperatures leads to the development of higher concentration gradients near the steel surface, so that the supersaturation required for the precipitation at the steel surface is reached before the bulk solution. This is evidenced by the lower levels of bulk precipitation observed far away from the samples at the end of the tests at 60 ^{o}C, in contrast to 35 ^{o}C, where the precipitation happened on every surface inside the autoclave.

3.3 Electrochemical properties of corrosion scales

Figure 7a shows the polarization curves obtained in the standard solution for the samples pre-corroded in various conditions, and Figure 7b shows the average corrosion rate calculated from the electrochemical measurements. Corrosion potential (E_{corr}), corrosion current density (i_{corr}), anodic Tafel slopes (β_a), cathodic Tafel slope (β_c) and polarization resistance (R_p) are shown in Table 2.

The corrosion potential of the pre-corroded samples is shown to be shifted to nobler regions when compared to a non-corroded sample. This shift is noticeably greater for the samples pre-corroded at higher temperature (60 ^{o}C). The upward trend in the corrosion potential is indicative of the presence of a corrosion product layer formation at the steel-electrolyte interface. Also, no signs of passivation could be observed for the anodic potential range scanned.

No discernible difference was evident between the samples pre-corroded at 35 ^{o}C, suggesting that neither the Ca^{2+} content up to 5000 ppm nor the longer exposure time (from 48 to 96 h) influenced the anodic or cathodic reaction process in this environment. This is supported by SEM morphology observations discussed previously, where no major morphology change was detected despite the longer exposure time at 35 ^{o}C. However, the samples pre-corroded at 60 ^{o}C exhibited potentiodynamic curves shifted to lower current densities indicating a certain degree of corrosion resistance when compared to the non-corroded sample. Secondly, the anodic Tafel slope (β_a) decreased for higher Ca^{2+} contents, indicating that the anodic reaction was accelerated by the addition of Ca^{2+}.

The potentiodynamic polarization curves seem to overlap for the samples pre-corroded at 35 ^{o}C, suggesting that neither the Ca^{2+} content up to 5000 ppm nor the longer exposure time (from 48 to 96 h) influenced the anodic or cathodic reaction process in this environment. However, the samples pre-corroded at 60 ^{o}C exhibited potentiodynamic curves shifted to lower current densities and higher potentials, indicating a higher degree of corrosion resistance when compared to the samples pre-corroded at lower temperatures.

The corrosion rate slightly decreased for longer exposure times and higher Ca^{2+} content in the brine (Figure 7b). The corrosion rate of the samples covered by a scale formed after 48 and 96 h dropped from 1.49 to 1.11 and 1.36 to 0.96 mm/year, when immersed in a brine containing 0 and 5000 ppm of Ca^{2+} respectively. Previous authors have linked the reduction in corrosion rate over time in CO_2 rich environments to the formation of dense crystalline $FeCO_3$ layers capable of blocking active sites on the surface of the sample and acting as a diffusion barrier to species involved in the cathodic reaction. This layer can protect the sample surface, by reducing the rate of the electrochemical reactions taking place on the surface, reducing the corrosion rate [13]. The results show similar behaviour for steel covered by a mixed iron-calcium carbonate ($Fe_xCa_yCO_3$)

corrosion product scale. Furthermore, the corrosion rate was shown to decrease even in the absence of a crystalline corrosion product scale, where the samples pre-corroded for 48 h exhibited similar behaviour despite being covered by a largely amorphous layer.

The values calculated from the electrochemical measurements cannot be readily compared to those measured using mass loss technique, because: (i) the electro-chemical measurements were carried out under different thermodynamic conditions compared to the condition where the corrosion scales were formed, and also (ii) because the data obtained from mass loss tests are an average for the whole test period, while the electrochemical measurements show instantaneous values at the end of the test period. Despite this, the individual results demonstrate how the corrosion rate changes over time.

Figure 8 shows the relative reduction in corrosion rate when increasing the Ca^{2+} content in the brine. It shows similar behaviour for both measurement techniques at 35 ^{o}C, indicating that both average (mass loss measurement) and instantaneous (electrochemical) values follow the same trend. However, the results at 60 ^{o}C diverge, implying that the enhanced reaction rate induced by the higher temperature in the first few hours made the corrosion rate so high that it shifted the average corrosion rate to higher values. This supports the earlier suggestion that the mass loss measurements may not be an accurate reflection of the corrosion rate in the presence of a protective corrosion product scale, i.e., the corrosion rate under these conditions is over-estimated, and is not a good indicator of true scale protectiveness.

4 CONCLUSIONS

The role of Ca^{2+} content in the brine on the corrosion behaviour of X80 carbon steel in a CO_2-saturated brine at 35 and 60 ^{o}C for 48 and 96 h at 80 bar was evaluated using mass loss, electrochemical and surface analysis techniques. The presence of Ca^{2+} in the brine favoured the precipitation of a mixed iron-calcium carbonate ($Fe_xCa_yCO_3$, where x+y=1) scale with increasingly calcium molar mass, shifting the carbonate crystals morphology from prismatic crystals to a globular structure. Results also showed the presence of Ca^{2+} slightly reduced the average corrosion rate even in the absence of a crystalline corrosion product scale. But the presence of a mixed iron-calcium carbonate scale offered better protectiveness to the carbon steel when compared to the pure iron carbonate. At higher temperatures (60 ^{o}C) it is believed that the barrier effect produced by the thicker and more compact carbonate scale had a greater influence in reducing the measured corrosion rate.

5 ACKNOWLEDGMENTS

The authors would like to acknowledge the funding from CNPq (National Council for Scientific and Technological Development/Brazil) and Shell (Brazil), which made this research possible.

6 REFERENCES

1. Shamsa, A., R. Barker, Y. Hua, E. Barmatov, T.L. Hughes, and A. Neville, Corros Sci 156 (2019): pp. 58–70, https://linkinghub.elsevier.com/retrieve/pii/S0010938X18323710.

2. Hua, Y., A. Shamsa, R. Barker, and A. Neville, Appl Surf Sci 455 (2018): pp. 667–682, https://linkinghub.elsevier.com/retrieve/pii/S0169433218314545.
3. Barker, R., Burkle, D., Charpentier, T., Thompson, H., and Neville, A., Corros Sci 142 (2018): pp. 312–341, https://doi.org/10.1016/j.corsci.2018.07.021.
4. Wei, L., X. Pang, C. Liu, and K. Gao, Corros Sci 100 (2015): pp. 404–420, https://linkinghub.elsevier.com/retrieve/pii/S0010938X15300482.
5. Zhang, Y., X. Pang, S. Qu, X. Li, and K. Gao, Corros Sci 59 (2012): pp. 186–197, https://linkinghub.elsevier.com/retrieve/pii/S0010938X12001059.
6. Sun, W., and S. Nešić, CORROSION 64 (2008): pp. 334–346, http://corrosionjournal.org/doi/10.5006/1.3278477.
7. Zhang, Y., X. Pang, S. Qu, X. Li, and K. Gao, International Journal of Greenhouse Gas Control 5 (2011): pp. 1643–1650, https://linkinghub.elsevier.com/retrieve/pii/S1750583611001812.
8. Tavares, L.M., E.M. da Costa, J.J. de O. Andrade, R. Hubler, and B. Huet, Appl Surf Sci 359 (2015): pp. 143–152, https://linkinghub.elsevier.com/retrieve/pii/S0169433215024940.
9. Ding, C., K. Gao, and C. Chen, International Journal of Minerals, Metallurgy and Materials 16 (2009): pp. 661–666, http://dx.doi.org/10.1016/S1674-4799(10)60009-X.
10. Mansoori, H., B. Brown, D. Young, S. Nešić, and M. Singer, Corrosion 75 (2019): pp. 1434–1449, https://meridian.allenpress.com/corrosion/article/75/12/1434/445378/Effect-of-FexCayCO3-and-CaCO3-Scales-on-the-CO2.
11. Cui, G., Yang, Z.Q., Liu, J.G., Li, .Z.L, International Journal of Greenhouse Gas Control 90 (2019): pp. 102814, https://doi.org/10.1016/j.ijggc.2019.102814.
12. Mansoori, H., D. Young, B. Brown, and M. Singer, J Nat Gas Sci Eng 59 (2018): pp. 287–296, https://linkinghub.elsevier.com/retrieve/pii/S187551001830369X.
13. Esmaeely, S.N., Y.-S. Choi, D. Young, and S. Nešić, Corrosion 69 (2013): pp. 912–920, https://meridian.allenpress.com/corrosion/article/69/9/912/163201/Effect-of-Calcium-on-the-Formation-and.
14. Esmaeely, S.N., D. Young, B. Brown, and S. Nešić, CORROSION 73 (2017): pp. 238–246, http://corrosionjournal.org/doi/10.5006/2261.
15. ASTM G1, "Standard Practice for Preparing, Cleaning, and Evaluation Corrosion Test Specimens," ASTM International (2017).
16. Nesic, S., J. Postlethwaite, and S. Olsen, CORROSION 52 (1996): pp. 280–294, http://corrosionjournal.org/doi/10.5006/1.3293640.
17. ASTM G102, "Standard Practice for Calculation of Corrosion Rates and Related Information from Electrochemical Measurements," ASTM International (2015).
18. Nešić, S., and K.-L.J. Lee, CORROSION 59 (2003): pp. 616–628, http://corrosionjournal.org/doi/10.5006/1.3277592.
19. Sun, W., S. Nešić, and R.C. Woollam, Corros Sci 51 (2009): pp. 1273–1276, https://linkinghub.elsevier.com/retrieve/pii/S0010938X09000961.

7 FIGURE CAPTIONS

FIGURE 1. Schematic diagram of the test setup showing the samples attached to the holder.

FIGURE 2. XRD patterns collected from X80 carbon steel exposed to a CO2-saturated brines at 80 bar for different exposure times and brine composition, (a) 0 ppm, (b) 1000 ppm, (c) 5000 ppm Ca^{2+} for 48 h at 35 ^{o}C, (d) 0 ppm, (e) 1000 ppm, (f) 5000 ppm Ca^{2+} for 96 h at 35 ^{o}C, (g) 0 ppm, (h) 1000 ppm, (i) 5000 ppm Ca^{2+} for 96 h at 60 ^{o}C.

FIGURE 3. SEM images of X80 carbon steel exposed to a CO_2-saturated brines at 80 bar for different exposure times and brine composition, (a) 0 ppm, (b) 1000 ppm, (c) 5000 ppm Ca^{2+} for 48 h at 35 °C, (d) 0 ppm, (e) 1000 ppm, (f) 5000 ppm Ca^{2+} for 96 h at 35 °C, (g) 0 ppm, (h) 1000 ppm, (i) 5000 ppm Ca^{2+} for 96 h at 60 °C.

FIGURE 4. SEM cross-section images and associated EDX area scans of X80 carbon steel exposed to a CO_2-saturated brines with different composition, (a) 0 ppm, (b) 1000 ppm, (c) 5000 ppm Ca^{2+} at 35 °C and 80 bar for 96 h.

FIGURE 5. SEM cross-section images and associated EDX area scans of X80 carbon steel exposed to a CO_2-saturated brines with different composition, (a) 0 ppm, (b) 1000 ppm, (c) 5000 ppm Ca^{2+} at 60 °C and 80 bar for 96 h.

FIGURE 6. (a) Average corrosion rate determined from mass loss measurements and (b) total scale mass as a function of time and Ca^{2+} content in the brine for X80 carbon steel exposed to a CO_2-saturated brine at 35 or 60 °C and 80 bar.

FIGURE 7. (a) Potentiodynamic polarization curves for scales and (b) average corrosion rate calculated from electrochemical measurements in 30g/L NaCl solution at 25 °C of X80 steel samples pre-corroded at 35 or 60 °C and 80 bar in brines containing 0 to 5000 ppm Ca^{2+}.

FIGURE 8. Relative corrosion rate from (a) mass loss measurements and (b) electrochemical measurements in brines containing 0 to 5000 ppm Ca^{2+}.

8 TABLES

TABLE 1. Test matrix for corrosion tests in scCO_2-saturated water.

Test No.	Temperature (°C)	Pressure (bar)	Brine composition		Test duration (h)
			NaCl (g/L)	$CaCl_2 \cdot 2H_2O$ (g/L)	
1	35	80	30.00	0	48
2			27.08	3.67	
3			15.42	18.34	
4			30.00	0	96
5			27.08	3.67	
6			15.42	18.34	
7	60		30.00	0	96
8			27.08	3.67	
9			15.42	18.34	

TABLE 2. Potentiodynamic electrochemical parameters for the corrosion of X80 steel in 30g/L NaCl solution at 25 °C.

Pre-corrosion condition				E_{corr} (mV) vs Ag/AgCl	i_{corr} (mA/cm^2)	β_a (mV/dec)	β_c (mV/dec)	R_p (Ohm*cm^2)
Ca^{2+} (ppm)	T (°C)	t (h)	P (bar)					
Non-corroded sample				-675	0.071±0.003	80	600	184±8
0	35	48	80	-643	0.149±0.012	61	277	169±4
1000				-642	0.109±0.018	56	225	170±12
5000				-642	0.094±0.020	55	225	208±31
0		96		-635	0.116±0.023	55	220	168±34

1000				-636	0.111±0.032	75	180	216±63
5000				-640	0.084±0.007	50	250	221±19
0				-579	0.0065±0.0001	105	250	4922±96
1000	60			-587	0.0061±0.0001	100	420	5790±245
5000				-587	0.0049±0.0001	70	500	5428±82

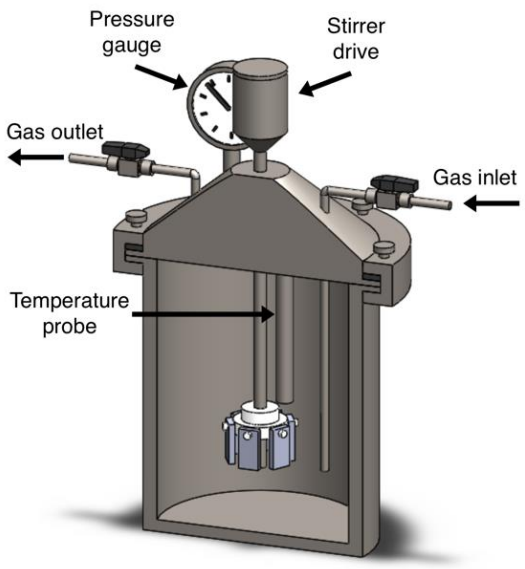

FIGURE 1. Schematic diagram of the test setup showing the samples attached to the holder.

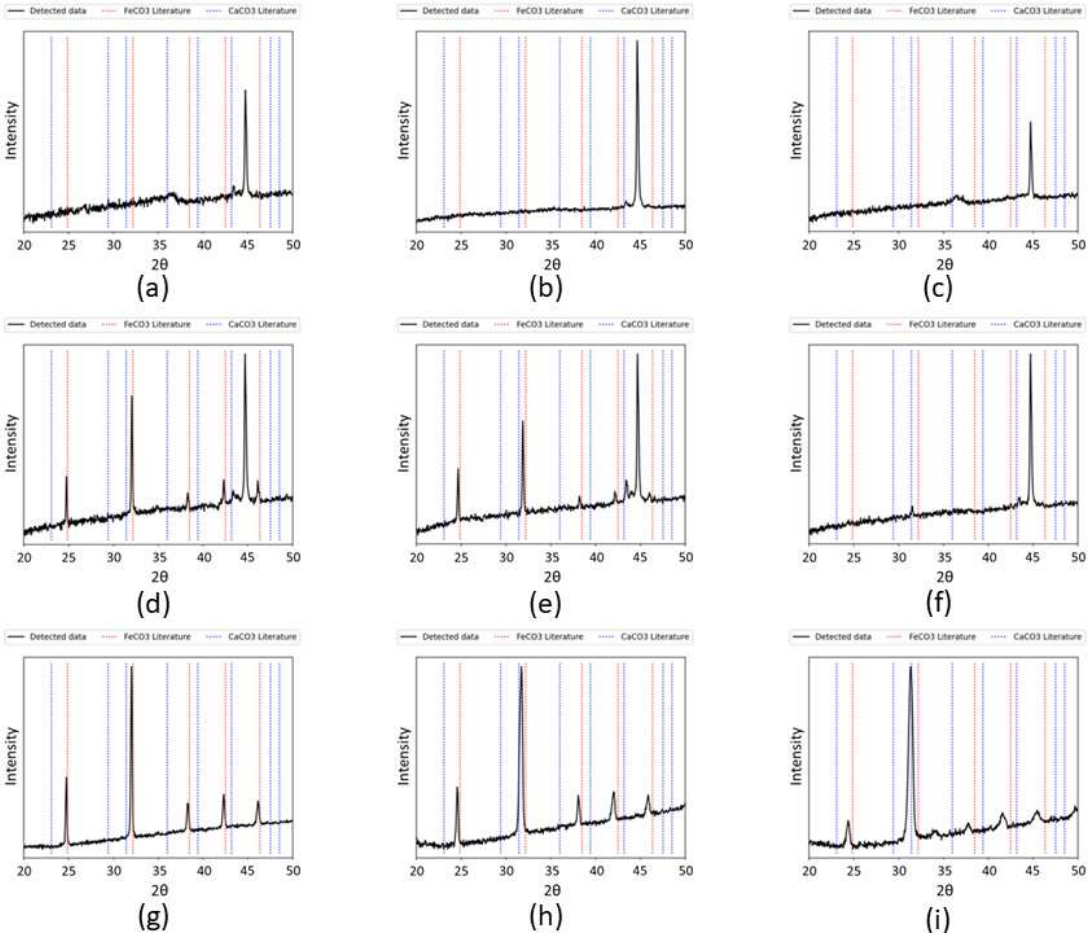

FIGURE 2. XRD patterns collected from X80 carbon steel exposed to a CO2-saturated brines at 80 bar for different exposure times and brine composition, (a) 0 ppm, (b) 1000 ppm, (c) 5000 ppm Ca^{2+} for 48 h at 35 ^{o}C, (d) 0 ppm, (e) 1000 ppm, (f) 5000 ppm Ca^{2+} for 96 h at 35 ^{o}C, (g) 0 ppm, (h) 1000 ppm, (i) 5000 ppm Ca^{2+} for 96 h at 60 ^{o}C.

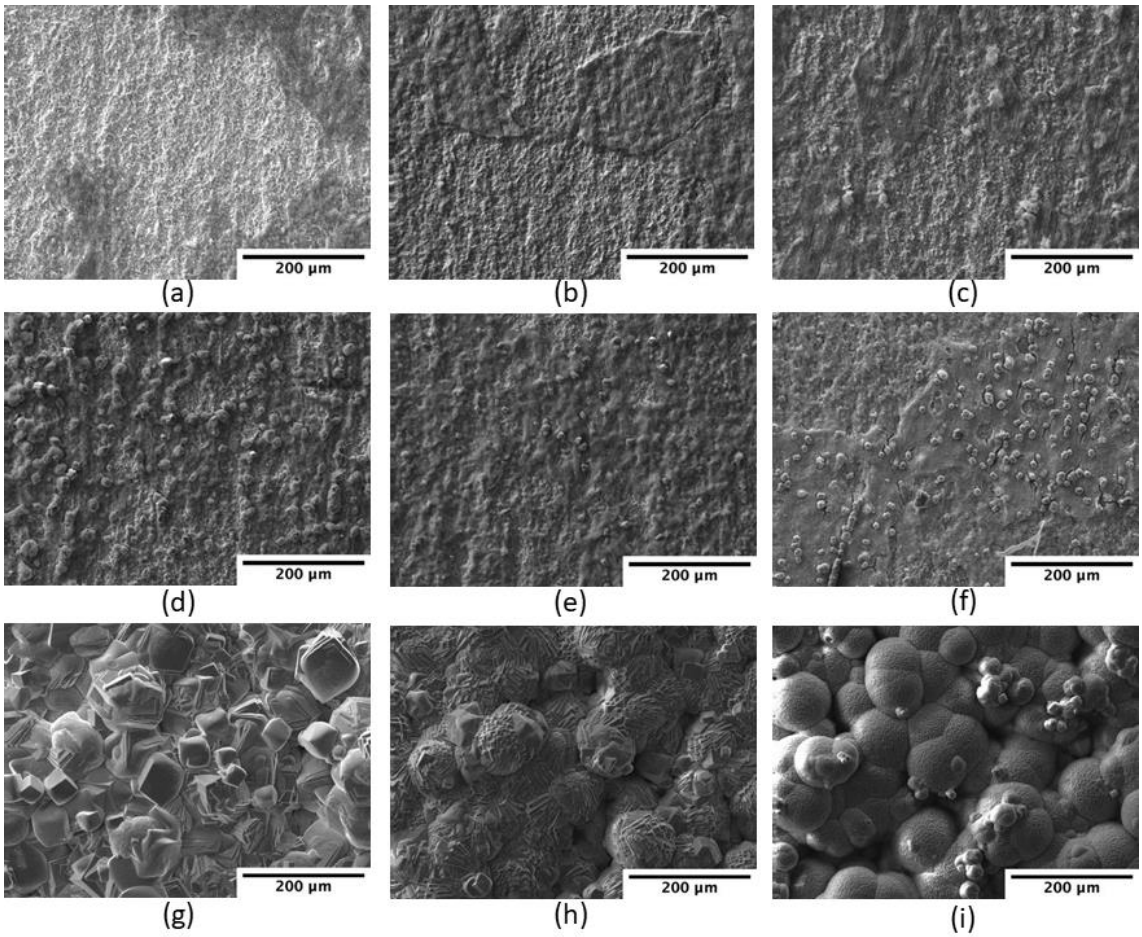

FIGURE 3. SEM images of X80 carbon steel exposed to a CO_2-saturated brines at 80 bar for different exposure times and brine composition, (a) 0 ppm, (b) 1000 ppm, (c) 5000 ppm Ca^{2+} for 48 h at 35 ^{o}C, (d) 0 ppm, (e) 1000 ppm, (f) 5000 ppm Ca^{2+} for 96 h at 35 ^{o}C, (g) 0 ppm, (h) 1000 ppm, (i) 5000 ppm Ca^{2+} for 96 h at 60 ^{o}C.

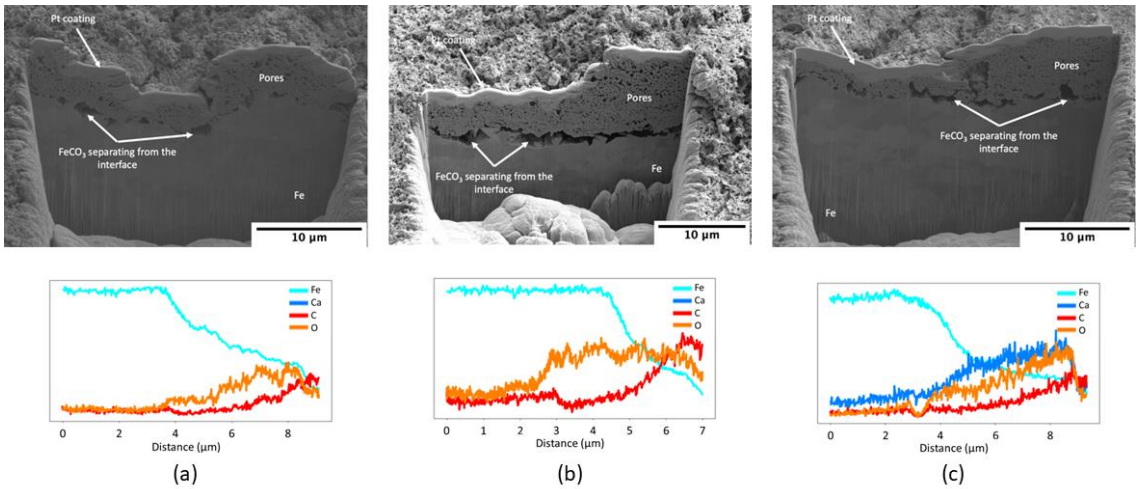

FIGURE 4. SEM cross-section images and associated EDX area scans of X80 carbon steel exposed to a CO_2-saturated brines with different composition, (a) 0 ppm, (b) 1000 ppm, (c) 5000 ppm Ca^{2+} at 35 °C and 80 bar for 96 h.

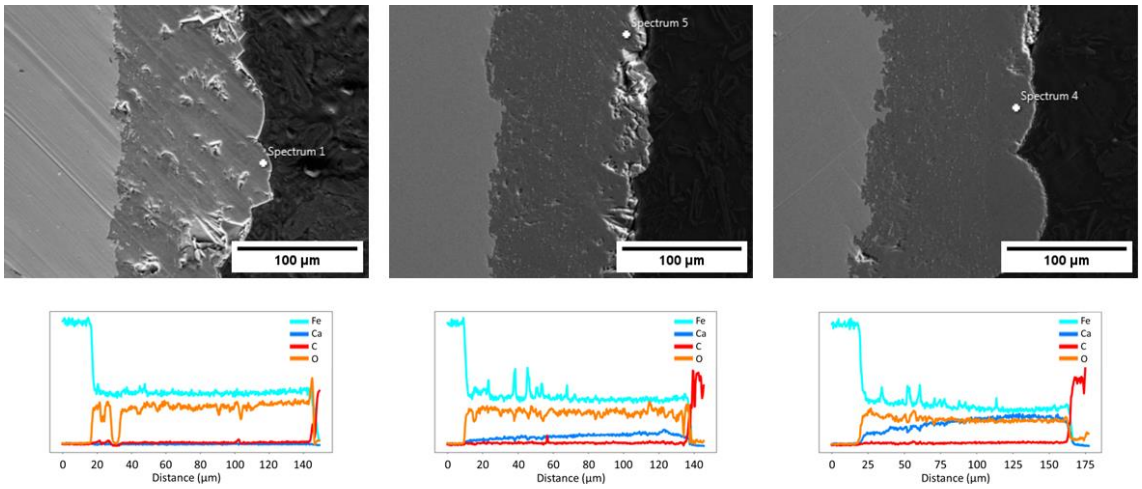

(a) (b) (c)

FIGURE 5. SEM cross-section images and associated EDX area scans of X80 carbon steel exposed to a CO_2-saturated brines with different composition, (a) 0 ppm, (b) 1000 ppm, (c) 5000 ppm Ca^{2+} at 60 ^{o}C and 80 bar for 96 h.

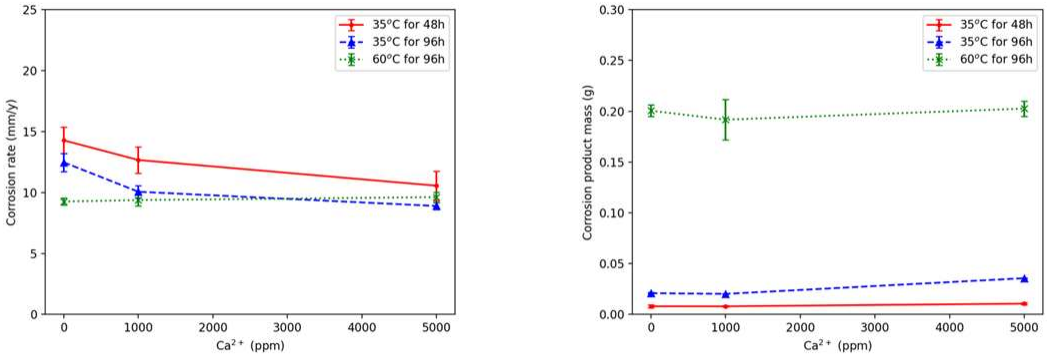

(a) (b)

FIGURE 6. (a) Average corrosion rate determined from mass loss measurements and (b) total scale mass as a function of time and Ca^{2+} content in the brine for X80 carbon steel exposed to a CO_2-saturated brine at 35 or 60 °C and 80 bar.

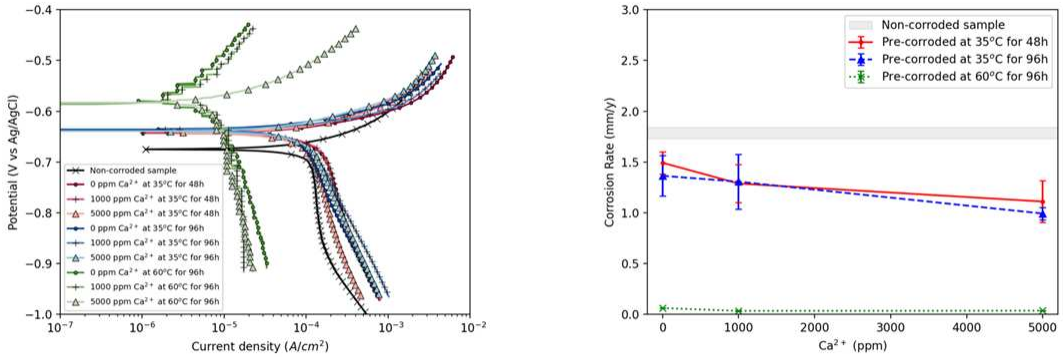

(a) (b)

FIGURE 7. (a) Potentiodynamic polarization curves for scales and (b) average corrosion rate calculated from electrochemical measurements in 30g/L NaCl solution at 25 °C of X80 steel samples pre-corroded at 35 or 60 °C and 80 bar in brines containing 0 to 5000 ppm Ca^{2+}.

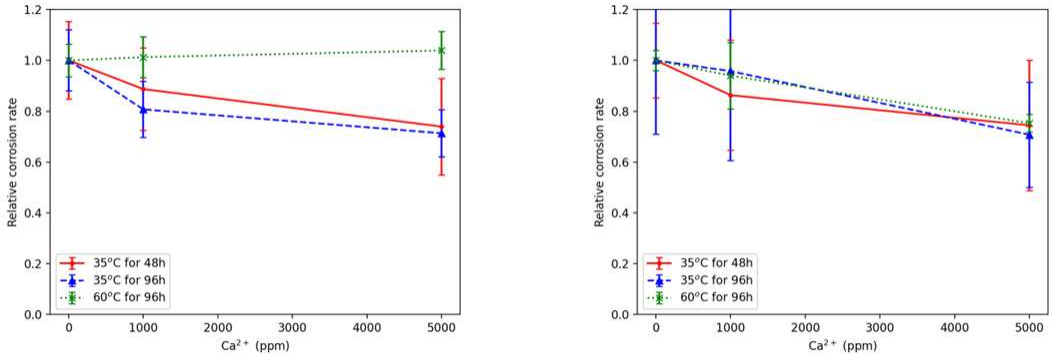

FIGURE 8. Relative corrosion rate from (a) mass loss measurements and (b) electrochemical measurements in brines containing 0 to 5000 ppm Ca^{2+}.